UNIVERSITY OF STUTTGART

MASTER'S THESIS

Dipolar Quantum Gases under Rotation

Author:
Ninaad ADHVARYU

Supervisor:
Dr. Tilman PFAU

A thesis submitted in fulfillment of the requirements for the degree Master of Physics

at the

Pi5
Department of Physics, University of Stuttgart

September 30, 2023

Declaration of Authorship

I,Ninaad ADHVARYU, hereby declare that the thesis titled "Dipolar Quantum Gases under Rotation" and its contents are entirely my own work, conducted during my research degree at University of Stuttgart .

I have acknowledged any prior submissions of portions of this thesis for academic qualifications, always providing clear attribution when consulting or quoting the work of others.

In cases where this thesis is based on collaborative efforts, I have distinctly delineated the contributions of others and my own. Furthermore, I have duly recognized all significant sources of assistance received during the research process.

Signed:

Date:

"We can see how the whole becomes not only more than but very different from the sum of the parts."

Philip Warren Anderson

UNIVERSITY OF STUTTGART

Abstract

Tilman Pfau

Department of Physics, University of Stuttgart

Master of Physics

Dipolar Quantum Gases under Rotation

by Ninaad ADHVARYU

This thesis examines the behavior of dipolar Bose-Einstein condensates, focusing on vortex formation induced by angular velocity. We discuss the atomic interactions present within dipolar gases and the influence of rotation on condensate dynamics. We develop a Gross-Pitaveskii equation that decribes these factors. Then we discuss the implimentation of the Conjugate Gradient Method and the Imaginary Time Evolution Method for efficient numerical solutions. Finally, we validate the ground state calculations, explore numerical acceleration techniques, and evaluate spatial resolution effects on ground state energies.

Contents

Chapter 1

Introduction

The creation, arrangement and characteristics of vortices is an important area of study across a wide range of physics. They are essential in understanding the effects of rotation in a classical fluid. As a result, they make up a significant part of the study of turbulence, where they are characterised by *circulation* and *vorticity*. Unlike classical vortices, quantum vortices cannot take an arbitrary value of circulation and are instead *quantised*.

Quantised vortices are a key observation in the detection of superfluidity, a phenomenon closely related to Bose-Einstein condensation (BEC). These quantised vortices were first observed in superfluid Helium [31], though they have subsequently been observed in Bose-Einstein condensates, non-linear optics and type-II superconductors. The prediction of quantised vortices was first made by Onsager, later extended by Feynman in 1955 [20], and by Abrikosov in 1957 [2].

Though first observed in superfluid Helium, current studies of quantum vortices focuses on ultracold gases, or BECs. These were first observed by Ketterle and Dalibard [28, 1].

Most studies of quantised vortices have been done in BEC systems with only short ranged contact interactions. Dipolar gases have an anisotropic nature, the formation and observation of quantised vortices within these gases opens up new and exotic phases of dilute quantum gases.

In this thesis, we explore the formation and organization of these vortices using the extended Gross-Pitaevskii Equation (eGPE). While the standard GPE provides a mean-field description, the eGPE incorporates quantum fluctuations, crucial in preventing the collapse of dipolar BECs [15]. This inclusion is realized through the Lee-Huang-Yang (LHY) correction term.

The eGPE cannot be solved exactly and must be calculated through numerical methods. Ground-state search is conducted via, Conjugate Gradient and Imaginary Time evolution methods. The inclusion of the rotating term in the eGPE requires modifications to algorithms.

This work aims to investigate the behaviour of quantized vortices in dipolar BECs, the formation and spatial arrangements of ground-states.

Chapter 2

Rotating Dipolar BEC Theory

To investigate the effects of rotation on a Dysprosium Bose-Einstein condensate, we need to understand the Gross-Pitaevskii equation and its extensions. Additionally, we should understand the anisotropic effects of an atom with a large magnetic moment and the physics of vortices in a superfluid.

2.1 Ideal Bose Gas

Our theoretical study of BECs begins with the analysis of the ideal, non-interacting Bose gas.

A Bose gas is composed of bosons, identical particles with wave-function symmetric under exchange. To understand the probability distribution of the microscopic states of a Bose gas, we consider the grand canonical ensemble. In this ensemble, the system can exchange energy and particles with a reservoir while maintaining a fixed temperature, T, and fixed chemical potential, μ.

The ideal Bose gas is presumed to have a correlation length much shorter than the density variations across the gas.

The distribution function of a system of bosons

$$n_i = \frac{g_i}{e^{\frac{\epsilon_i - \mu}{k_B T}} - 1} \tag{2.1}$$

is characterised by energy levels ϵ_i, degeneracy g_i, and n_i bosons.

The system described by Equation 2.1 is constrained by

$$\sum_i n_i = N; \quad \sum_i \epsilon_i n_i = U \tag{2.2}$$

where, N is total number of particles and U is total energy

Now, we transition from the discussion of discrete energy levels to continuous energy levels, switching from a sum over states to an integral,

$$N \approx \int d\epsilon \frac{1}{e^{\frac{\epsilon-\mu}{k_B T}} - 1} g(\epsilon) \tag{2.3}$$

where ϵ is the density of states, we have also set the degeneracy to 1.

The density of states for a three-dimensional homogeneous system is

$$g(\epsilon) = V \frac{\sqrt{2}}{3\pi^2\hbar^3} (m)^{\frac{3}{2}} \sqrt{\epsilon} \tag{2.4}$$

where V is the volume and m is the mass.

We will now explore how Equation 2.3 behaves when additional particles are introduced into the system, while keeping the temperature fixed.

By combining Equations 2.3 and 2.4, we can express the density

$$n = \frac{N}{V} = \frac{m^{\frac{3}{2}}}{\sqrt{2}\pi^2\hbar^3} \int d\epsilon \frac{\epsilon^{\frac{1}{2}}}{e^{\frac{\epsilon-\mu}{k_B T}}} \tag{2.5}$$

As the density increases, μ must also increase, while remaining negative.

Leading to

$$\begin{aligned} n(\mu = 0) &= \frac{m^{\frac{3}{2}}}{\sqrt{2}\pi^2\hbar^3} \int d\epsilon \frac{\epsilon^{\frac{1}{2}}}{e^{\frac{\epsilon-\mu}{k_B T}}} \\ &= \frac{m^{\frac{3}{2}}}{\sqrt{2}\pi^2\hbar^3} (k_B T)^{\frac{3}{2}} \int dx \frac{\sqrt{x}}{e^x - 1} \end{aligned} \tag{2.6}$$

where $x = \frac{\epsilon}{k_B T}$.

The evaluation of Equation 2.6

$$n_c = \Gamma(3/2)\zeta(3/2) \frac{m^{\frac{3}{2}}}{\sqrt{2}\pi^2\hbar^3} \tag{2.7}$$

is in term of Gamma function Γ and the Riemann zeta function ζ.

However, this expression shows the density of states is bounded and independent of the particle number.

The underlying issue arises from Equation 2.3 when transitioning from discrete to continuous states. The transition, as currently formulated, does not hold when the density of states approaches zero. This can be rectified by considering the lowest energy state in addition to other excited states, yielding $n = n_0 + n_{\text{ex}}$

$$n_0 = \frac{1}{V}\frac{1}{e^{\frac{-\mu}{k_B T}} - 1};\ n_{ex} = \frac{m^{\frac{3}{2}}}{\sqrt{2}\pi^2\hbar^3}\int d\epsilon \frac{\epsilon^{\frac{1}{2}}}{e^{\frac{\epsilon-\mu}{k_B T}}} \tag{2.8}$$

As new particles are added μ must approach zero and n_{ex} is bound as seen in Equation 2.7 and n_0 grows without an upper-bound. Physically, any new particles added to the system, over the critical density, must then go to ground-state. This is Bose-Einstein condensation.

The critical density, n_c can be expressed as the thermal de-Broglie wavelength, λ_T^3

$$n_c = 2.3\frac{2}{\sqrt{\pi}}\frac{1}{\lambda_T^3} \tag{2.9}$$

Physically, this can be understood to be how far the wave-function of particles extends in real space.

We can understand that the phenomenon of BEC will occur as the inter particle distance approaches the de Broglie wavelength, with critical temperature

$$T_c = 3.31\frac{\hbar^2 n^{\frac{2}{3}}}{m k_B} \tag{2.10}$$

and condensate fraction

$$n_0 = 1 - \left(\frac{T}{T_c}\right)^{\frac{3}{2}} \tag{2.11}$$

2.2 Atomic Interactions

At low temperatures, an interacting atomic system exhibits behaviours that significantly impact its phase and properties. One of the key phenomena that occur in such conditions is three-body recombination, wherein three atoms come together and form molecules. This process has a significant influence on the system, often shifting it towards a solid state of matter due to the formation of molecular structures.

A BEC phase is only meta-stable for interacting atoms if the density remains sufficiently low to prevent three-body interactions. When the atoms are more dilute, with a typical inter-atomic spacing of the order of 10^2 nm [33], two-body interactions tend to dominate the behaviour of the system.

The prevalent two-body interactions in such dilute atomic gases can be effectively modelled using s-wave scattering theory. This theory allows for a mathematical understanding of the collisions between two atoms and offers valuable insights into the interactions that occur at the atomic level.

2.2.1 Contact Interaction

The behaviour of neutral atoms in a Bose-Einstein Condensate (BEC) is influenced by the Van der Waals force between atoms, typically described by the Lennard-Jones potential

$$V(\mathbf{r}) = \frac{A}{r^{12}} - \frac{B}{r^6} \tag{2.12}$$

where r is the inter-particle distance and A and B are species-specific constants. First term is an overlap of electron orbitals leading to an electrostatic repulsion, the second term describes the long-range interaction.

However, Equation 2.12 contains many solutions which are not relevant to our system (ie. scattering states), thus we aim to reduce the LJ potential into a *pseudo-potential*.

In the absence of relativistic spin-spin and spin-orbital interactions, the Schrödinger equation for two colliding atoms can be written as [34]

$$\left(\frac{-\hbar^2}{2m_r}\nabla + V(\mathbf{r}) - E\right)\psi(\mathbf{r}) = 0 \tag{2.13}$$

where $\mathbf{r}$ is the relative distance between particles, and m_r is the reduced mass.

We use the Ansatz, a sum of the incoming wave and the scattered wave.

$$\psi(r\mathbf{r}) = e^{i\mathbf{k}\cdot\mathbf{r}} + \psi_{scat.wave} \tag{2.14}$$

The $\psi_{scat.wave}$ part of Equation 2.14 depends only on the angle θ of the two particles after collision, simplifying Equation 2.14

$$\psi = e^{i\mathbf{k}\cdot\mathbf{r}} + f(\theta)\frac{e^{ikr}}{r} \tag{2.15}$$

assuming $f(\theta)$ is constant due to low energy state conditions, written in terms of the *scattering length a*

$$\psi = 1 - \frac{a}{r} \tag{2.16}$$

The differential cross section, representing elastic collisions between atoms, is

$$d\sigma = |f(\theta)|^2 \sin\theta d\theta d\phi \tag{2.17}$$

For identical bosons, the equation simplifies further,

$$d\sigma = |f(\theta) + f(\pi - \theta)|^2 \, d\Omega \tag{2.18}$$

The total scattering cross-section for a polarized boson is given by integrating over all possible final states. The symmetric nature of Equation 2.18 , means we integrate over half the 4π solid angle,

$$\sigma = 8\pi a^2 \tag{2.19}$$

This can be inserted into the pseudo-potential,

$$V_s(r) = g_s \cdot \delta(r) \tag{2.20}$$

why this form of pseudo-potential can be applied to this situation can be found in [33].

where δ is the Dirac delta, and g_s is defined

$$g_s = \frac{4\pi\hbar^2}{m} a_s \tag{2.21}$$

The entire contact interaction can is described by varying the scattering length a_s, which can be positive or negative- depending on Feshbach resonances.

2.2.2 Dipolar Interaction

Dysprosium atoms in the ground state possess a large magnetic moment ($\mu_m \approx 10\mu_B$) and experience the magnetic dipole-dipole interaction, also known as dipolar interaction. In contrast to the short-range contact interaction this is anisotropic and long-range [17].

To achieve alignment of dipoles, an external magnetic field is applied, resulting in polarization of the atom cloud.

Dipole-dipole interaction potential, $V_{dd}(r, \theta)$,

$$V_{dd}(r, \theta) = \frac{\mu_0 \mu_m^2}{4\pi} \frac{1 - 3\cos^2\theta}{r^3} \tag{2.22}$$

where r is the relative distance between dipoles, θ is the angle between the external magnetic field and the dipole, μ_0 is the magnetic permeability of vacuum.

The anisotropy of the interaction arises due to the $cos^2\theta$ term in the potential equation. This means that the potential may be attractive or repulsive, depending on the relative angle between dipoles. This anisotropy changes sign at the "magic angle" $\theta_m = \arccos\left(\frac{1}{\sqrt{3}}\right)$. Shape of the trap plays a vital role in maintaining or collapsing a dipolar BEC. A trap that is elongated along the axis of polarization will, for instance, be prone to collapse as the dipoles will have a large attractive potential [17].

Analogous to 2.21 the dipolar coupling strength is

$$g_{dd} = \frac{4\pi\hbar^2}{m} a_{dd} \tag{2.23}$$

where characteristic length scale for the dipolar interaction is

$$a_{dd} = \frac{\mu_0 \mu_m^2 m}{12\pi\hbar^2} \tag{2.24}$$

with m as the mass, μ_0 is vacuum permeability and μ_m is the magnetic moment.

An interaction ratio ϵ_{dd} between the dipolar and contact interactions can be defined

$$\epsilon_{dd} = \frac{a_{dd}}{a_s} = \frac{\mu_0 \mu_m^2 m}{12\pi\hbar^2 a_s} \tag{2.25}$$

When $\epsilon_{dd} > 1$, the dipolar interaction dominates, leading to instability in a homogeneous BEC.

In the weak dipolar interaction limit (first order Born approximation), the effective potential is the sum of contact and dipolar potentials

$$V_{\text{int}}(r) = \frac{g_s}{2}\left(1 + \epsilon_{dd}\left(3\cos^2\theta - 1\right)\right) \tag{2.26}$$

The dipolar interaction, due to its long-range nature and anisotropy, significantly impacts the scattering problem. It involves all partial waves ($l > 0$) and cannot be reduced to a simple pseudo-potential. However, at low collision energies, dipolar scattering becomes universal and mainly involves s-wave channels. The Born approximation remains valid in this regime, allowing the total elastic scattering cross-sections to be conveniently added for identical bosons and fermions [19].

This thesis focuses on Dysprosium dipolar BECs, it's ground state angular momentum ($J = 8$) results in one of the largest permanent dipole moments among all elements, making each atom behave like an individual dipole.

In conclusion, the dipolar interaction in BECs is characterised by its anisotropic and long-range nature. Understanding its interplay with the contact interaction is essential for studying and manipulating ultracold quantum gases.

2.3 Gross-Pitaevskii Equation

In this section, we derive the Gross-Pitaevskii equation, a fundamental equation in understanding Bose-Einstein condensates (BECs).

Let's begin with the most general case. In a condensed system, all particles occupy the same single-particle state $\phi(r)$, satisfying normalization condition $\int d^3r|\psi(\mathbf{r})|^2 = 1$. The total wave function in a mean-field approximation is a symmetric product of the single-particle wave functions.

As this is a simple case, we define the mean-field energy as only contact interaction 2.21, leading to the total Hamiltonian

$$H = \sum_{i=1}^{N}\left(\frac{\mathbf{p}_i^2}{2m} + V_{ext}(\mathbf{r}_i)\right) + g_s\sum_{i<j}\delta(\mathbf{r}_i - \mathbf{r}_j) \tag{2.27}$$

To solve this Hamiltonian, we employ the variation method with an appropriate Ansatz. By minimizing the energy functional under variations of the wave function while keeping the total atom number constant, we obtain the time-independent Gross-Pitaevskii Equation

$$\mu\psi(\mathbf{r}) = \left(-\frac{\hbar^2}{2m}\nabla^2 + V_{ext}(\mathbf{r}) + g_s|\psi(\mathbf{r})|^2\right) \tag{2.28}$$

Our focus will extend beyond this fundamental form, incorporating *beyond mean-field* additions and dipolar terms, leading to an extended Gross-Pitaevskii Equation.

With inclusion of the interaction potential 2.26 Hamiltonian of the system transforms from 2.27 to

$$H = \int d\mathbf{r}\psi^\dagger(\mathbf{r})\left(\frac{\mathbf{p}_i^2}{2m} + V_{ext}(\mathbf{r}_i)\right)\psi(\mathbf{r}) + \frac{1}{2}\int d\mathbf{r}'\psi^\dagger(\mathbf{r})\psi^\dagger(\mathbf{r}')V_{int}(\mathbf{r}'-\mathbf{r})\psi(\mathbf{r}')\psi(\mathbf{r}) \tag{2.29}$$

Employing the assumption that for a ground state BEC the macroscopic occupation number is much larger than 1, it becomes possible to neglect parts of the ψ that are not condensed [14], and apply a treatment similar to the contact interaction approach to get the time-independent dipolar GPE (dGPE)

$$i\hbar\frac{\partial}{\partial t}\psi = \left(-\frac{\hbar^2}{2m}\nabla^2 + V_{ext} + g|\psi|^2 + \Phi_{dd}\right)\psi \tag{2.30}$$

with

$$\Phi_{dd} = \int d\mathbf{r}' V_{dd}(\mathbf{r}-\mathbf{r}')|\psi(\mathbf{r}')|^2 \tag{2.31}$$

This is a non-linear Schrödinger Equation.

So far, the physics has been based on mean-field theories however stable quantum droplet states with dysprosium have been observed [19]. To account for these experimental observations we modify the dGPE. Introducing *quantum fluctuations*, that shift the ground state density, n, and the μ [27].

The resultant extended GPE

$$i\hbar\frac{\partial}{\partial t}\psi = \left(-\frac{\hbar^2}{2m}\nabla^2 + V_{ext} + g|\psi|^2 + \Phi_{dd} + g_{qf}|\psi|^3\right)\psi \tag{2.32}$$

with

$$g_{qf} = \frac{32ga_s^{\frac{3}{2}}}{3\sqrt{\pi}}\left(1 + \frac{3}{2}\epsilon_{dd}\right) \tag{2.33}$$

This form of the GPE has been used recently in the discovery and research of quantum droplets[18, 22, 16, 37, 29, 32].

2.4 Rotation and Vortices

BECs and superfluids are both irrational fluids that form vortices upon the additional angular momentum. The vortex in this case can be thought of as can excitation that carries angular momentum, or a density hole with particles rotating around the core.

From equation 2.28, we can get the continuity equation, showing that the velocity field of the condensate is connected to the wave function.

$$\frac{\partial}{\partial t}|\psi|^2 = \frac{-i\hbar}{2m}\nabla\left(\psi * \nabla\psi + \psi\nabla\psi*\right) = 0 \tag{2.34}$$

which can be compared to the continuity question derived from the linear Schrödinger Equation

$$\frac{\partial}{\partial t}n + \nabla(n\mathbf{v}) = 0 \tag{2.35}$$

From this comparison we get the velocity field for the condensate as

$$\mathbf{v} = \frac{-i\hbar}{2m}\frac{\left(\psi * \nabla\psi + \psi\nabla\psi*\right)}{|\psi|^2} \tag{2.36}$$

where m is the mass.

Using the Ansatz, $\psi = fe^{i\phi}$, with f as the modulus and ϕ as the phase, we write the velocity field

$$\mathbf{v} = \frac{\hbar}{m}\nabla\phi \tag{2.37}$$

Importantly, the gradient of the phase of the wave function describes the velocity field of the condensate.

From classical physics, we define the measure *circulation*

$$\Gamma = \frac{h}{m}\int_A \nabla\times\nabla\phi = 0 \tag{2.38}$$

C is a contour that encloses the area A.

This equation implies that a superfluid cannot rotate.

The expression circulation of a superfluid is still valid in cases where the phase, ϕ, has a singularity. The change in the phase going around the contour must then be a multiple of 2π. The circulation becomes *quantised*

$$\Gamma = 2\pi l\frac{\hbar}{m} \tag{2.39}$$

where integer l is the winding number.

Rotating Frame

There are numerous methods to introduce vortices into a superfluid, an incomplete list includes cooling across a phase transition, perturbations via focused laser beams, artificial gauge fields [25, 11, 24, 30]. Angular momentum is included in the GPE by considering the rotation of the trapping potential in the laboratory frame. [26]

Let $\{\mathbf{e}_x, \mathbf{e}_y, \mathbf{e}_z\}$ denote the orthogonal basis for the three-dimensional space in which the trapping potential resides. The potential is rotated around the z-axis with an angular frequency Ω.

The transformation matrix for this rotation

$$R(t) = \begin{bmatrix} \cos(\Omega t) & -\sin(\Omega t) & 0 \\ \sin(\Omega t) & \cos(\Omega t) & 0 \\ 0 & 0 & 1 \end{bmatrix} \tag{2.40}$$

The primed unit vectors $\mathbf{e}_i' = R(t) \cdot \mathbf{e}_i$ describe the rotated frame. The time derivatives of these transformed unit vectors are expressed as

$$\frac{d}{dt}\mathbf{e}_i' = \dot{R}(t) \cdot \mathbf{e}_i \tag{2.41}$$

Using a substitution, $\tilde{R}(t) = \dot{R}(t) \cdot R^T(t)$, we define a new transformation matrix

$$\tilde{R}(t) = \Omega \begin{bmatrix} 0 & -1 & 0 \\ 1 & 0 & 0 \\ 0 & 0 & 1 \end{bmatrix} \tag{2.42}$$

Thus, Equation 2.41 can be simplified

$$\frac{d}{dt}\mathbf{e}_i' = \mathbf{e}_i{}' \times \Omega \tag{2.43}$$

For a vector $\mathbf{u} = u_i \cdot \mathbf{e}_i$ in the original three-dimensional space, its time derivative can be expressed as

$$\frac{d}{dt}\mathbf{u}(t) = \frac{d}{dt}u_i \cdot \mathbf{e}_i' + \Omega \times \mathbf{u}(t) \tag{2.44}$$

Extending this treatment to the wave function ψ, we can express its time derivative in the rotated frame as follows, employing the chain rule

$$\frac{\partial}{\partial t}\psi(\mathbf{x}, t) = \frac{\partial}{\partial t}\psi(\mathbf{x}', t) + (\Omega \times \mathbf{x}') \cdot \nabla\psi(\mathbf{x}', t) \tag{2.45}$$

The second term of Equation 2.45 can be simplified with the introduction of angular momentum operator $\mathbf{L} = -i\hbar(\Omega \times \mathbf{x}) \cdot \nabla$ and can be inserted into the extended GPE 2.32

$$i\hbar\frac{\partial}{\partial t}\psi = \left(-\frac{\hbar^2}{2m}\nabla^2 + V_{ext} + g|\psi|^2 + \Phi_{dd} + g_{qf}|\psi|^3 - \Omega L_z\right)\psi \tag{2.46}$$

Equation 2.46 the system we explore numerically.

Chapter 3

Numerical Methods

In the previous chapter, we developed the physics of a rotating, dipolar, BEC, which is described by a non-linear Schrödinger equation. This cannot be solved analytically and requires the use of numerical methods, we explore two different methods to find the ground state.

3.1 Conjugate Gradient Method

The Conjugate Gradient Method (CGM) is a widely employed iterative technique utilized to solve systems of linear equations,

$$Ax = b \tag{3.1}$$

where A represents a known square, symmetric, positive-definite matrix, b is a known vector, and x is an unknown vector.

This method is notably advantageous when A is sparse. A matrix is deemed positive-definite if, for any non-zero vector v, $v^T Av > 0$ (where v^T denotes the transpose of v), and all the eigenvalues of A are positive.

The precursor to the CGM is the steepest descent method. In its simplest form, it takes the system of linear equations as shown in Equation 3.1 and constructs a functional

$$f(x) = \frac{1}{2}x^T Ax - b^T x + c \tag{3.2}$$

A must be positive-definite as then surface described by Equation 3.2 parabolic. Our objective becomes locating the global minimum of this surface. The gradient is computed by taking the first-order derivative of Equation 3.2

$$f' = Ax - b \tag{3.3}$$

Steepest descent methods initiate at an arbitrary point x_0 and iteratively generate points x_i to approach the final solution x. Assuming we start far from x, Equation 3.3 will yield a non-zero value. To determine the next point x_1 such that we move along the steepest descent, two pieces of information are needed: the direction of steepest descent and an estimate of how far along that direction to move. Thus, we define

$$r = b - Ax \tag{3.4}$$

$$\alpha = \frac{\langle r|r\rangle}{\langle r, Ar\rangle} \tag{3.5}$$

Here, Equation 3.4 represents the residual and Equation 3.5 denotes the step size, obtained through a process known as line search. This allows us to calculate the next step x_i

$$x_i = x_{i-1} + \alpha_{x-1} r_{x-1} \tag{3.6}$$

This method exhibits a 'zig-zag' convergence towards the minimum due to the orthogonal nature of consecutive residuals, resulting in extended convergence times. This issue can be mitigated by first obtaining a residual from the initial guess and then creating a set of directions, orthogonal to the residue, to search for the next point. Another perspective is that, unlike the steepest descent method where we keep finding new residuals built from the previous ones through line searches, we are 'sweeping' across the entire space to find the steepest direction across a set of residuals, rather than one at a time. This significantly reduces the number of iterations required to approach the minimum.

The CGM begins by setting an initial guess x_0 and finding the first search direction

$$d_0 = b - Ax_0 \tag{3.7}$$

this is set as the first residual, $r_0 = d_0$.

Then, we begin a loop, finding the step size, α

$$\alpha_i = \frac{\langle r_i, r_i\rangle}{\langle d_i, Ad_i\rangle} \tag{3.8}$$

which is used for a new x

$$x_{i+1} = x_i + \alpha_i d_i \tag{3.9}$$

in turn gives a new residual

$$r_{i+1} = r_i + Ad_i \tag{3.10}$$

from which we define β, a parameter utilized to ascertain the conjugacy between the search directions in successive iterations of the CGM, ensuring that each search direction remains conjugate to the previous ones

$$\beta_{i+1} = \frac{\langle r_{i+1}, r_{i+1}\rangle}{\langle r_i, r_i\rangle} \tag{3.11}$$

the next search direction is found

$$d_{i+1} = r_{i+1} + \beta_{i+1} d_i \tag{3.12}$$

The process will loop till the successive results differ by less than the set criteria, in our case 10^{-14}. This method is most computationally expensive when having to do multiplication with matrix A.

This cost can be reduced through *preconditioning*. We want a matrix P such that the system can we re-written

$$P^{-1}Ax = P^{-1}b \tag{3.13}$$

with $\tilde{A} = P^{-1}A$. We select P such that $\tilde{A}$ has a condition number less than A. The condition number is a measure of how sensitive a system is to changes in input. Practically, we a looking for P that is symmetric and can approximate A.

The CGM is modified into the Preconditioned CGM by defining a new residual, $\tilde{r} = P^{-1}r$, and updating 3.7 - 3.13 into

$$d_0 = b - Ax_0 \tag{3.14}$$

$$\tilde{r_0} = P^{-1}d_0 \tag{3.15}$$

$$\alpha_i = \frac{\langle r_i, \tilde{r}_i \rangle}{\langle d_i, Ad_i \rangle} \tag{3.16}$$

$$x_{i+1} = x_i + \alpha_i d_i \tag{3.17}$$

$$r_{i+1} = r_i + Ad_i \tag{3.18}$$

$$\tilde{r}_{i+1} = r_i + Ad_i \tag{3.19}$$

$$\beta_{i+1} = \frac{\langle r_{i+1}, \tilde{r}_{i+1} \rangle}{\langle r_i, r_i \rangle} \tag{3.20}$$

$$d_{i+1} = \tilde{r}_{i+1} + \beta_{i+1} d_i \tag{3.21}$$

This is simply an intuition for the process of the Preconditioned CGM. The exact Algorithm 1 used has been adapted from [6].

Algorithm 1 The Preconditioned Conjugate Gradient Method

$n = 0$, given initial data $\boldsymbol{\phi}_n$
while not converged **do**
  $\mu_n = \langle H_{\boldsymbol{\phi}_n} \boldsymbol{\phi}_n, \boldsymbol{\phi}_n \rangle$
  $\boldsymbol{r}_n = H_{\boldsymbol{\phi}_n} \boldsymbol{\phi}_n - \mu_n \boldsymbol{\phi}_n$
  $\beta_n^{cg} = \mathrm{Re} \langle \boldsymbol{r}_n - \boldsymbol{r}_{n-1}, P\boldsymbol{r}_n \rangle \,/\, \langle \boldsymbol{r}_{n-1}, P\boldsymbol{r}_{n-1} \rangle$
  $\beta_n^{cg} = \max\left(\beta_n^{cg}, 0\right)$
  $d_n = -\mathrm{Pr}_n + \beta_n^{cg} p_{n-1}$
  $p_n = d_n - \mathrm{Re} \langle \boldsymbol{d}_n, \boldsymbol{\phi}_n \rangle \boldsymbol{\phi}_n$
  $\theta_n = \mathrm{argmin}_\theta \, \mathcal{E}\left(\cos(\theta)\boldsymbol{\phi}_n + \sin(\theta) p_n / \|p_n\|\right)$
  $\boldsymbol{\phi}_{n+1} = \cos(\theta_n)\, \boldsymbol{\phi}_n + \sin(\theta_n)\, p_n / \|p_n\|$
  $n = n + 1$
end while

For the rotated extended GPE, 2.46, the energy functional (3.2) is

$$E[\psi] = \int d\mathbf{r} \left(\frac{1}{2}|\nabla\psi|^2 + V_{ext}|\psi|^2 + \frac{1}{2} g_s |\psi|^4 + \frac{1}{2}|\psi|^2 (V_{dd} * |\psi|^2) + \frac{2}{5} g_{qf} |\psi|^5 - \Omega \psi^* L_z \psi \right) \tag{3.22}$$

The calculation of dipole interaction, 2.31, can be computed by find the product of $|\psi|^2$ and V_{dd} in momentum space. This is done via a fast Fourier transforms that assumes a periodic density distribution, to prevent computationally expensive and unnecessary long-range interaction we can employ a 'cut-off' dipolar interaction discussed in the Appendix of [36].

$$V_{\mathrm{dd}} = \left(-1 + 3 \cdot \hat{k} \cdot \hat{B}\right) \times \left(1 + 3 \times \frac{\cos(kR)}{(kR)^2} - \frac{\sin(kR)}{(kR)^3}\right) \tag{3.23}$$

To solve the minimization problem numerically, wave-function 2.46 needs to be discretized. Various approaches to the finding numerical discretisation of the standard and extended Gross-Pitaveskii Equation exist [8]. However, new challenges are introduced with the addition of the rotating term, the presence of the vortices mandates need for a finer grid, in order to resolve potential vortex lattices [9]. While various methods of discretisation have been followed for specific GPEs [7, 3, 4].

3.2 Imaginary Time Evolution

The imaginary time evolution method is a common approach for finding the ground states of BECs. It involves solving a time-independent Hamiltonian, which can be expressed as the sum of kinetic (T) and potential (V) energy operators: $H = T + V$.

The state $\psi(\mathbf{r}, t)$ can be described by the time-evolution operator, $e^{\frac{-i}{\hbar} tH}$ acting on $\psi(\mathbf{r}, t = 0)$

$$\psi(\mathbf{r}, t) = e^{\frac{-i}{\hbar} tH} \psi(\mathbf{r}, 0) \tag{3.24}$$

$\psi(\mathbf{r}, t = 0)$ can be decomposed into a sum of stationary states [1] ψ_i

$$\psi(\mathbf{r}, t) = \sum_i e^{\frac{-i}{\hbar} t E_i} \psi_i \tag{3.25}$$

where E_i is the eigen-energy of state ψ_i.

Changing the time variable to imaginary time $\tau = -it$, 3.25 becomes

$$\psi(\mathbf{r}, \tau) = \sum_i e^{\frac{-E_i}{\hbar} \tau} \psi_i \tag{3.26}$$

describing how the states ψ_i will reduce proportionally to their eigen-energies and converge to the lowest energy state, the ground state.

This technique can also be applied to non-linear Hamiltonians [10].

The operator $e^{\frac{-i}{\hbar} tH}$ from 3.24 is decomposed into kinetic and potential operators that can be applied sequentially to approximate a full time-step.

To handle the non-commutativity of kinetic and potential operators, we use the Baker-Hausdorff expansion and approximate

$$e^{\frac{-i}{\hbar} tH} \psi(\mathbf{r}, t) \approx e^{\frac{-i}{2\hbar} tT} e^{\frac{-i}{\hbar} tV} e^{\frac{-i}{2\hbar} tT} \psi(\mathbf{r}, t) \tag{3.27}$$

this is a second-order expansion known as Strang splitting.

Time Splitting

We split 2.46 into kinetic

$$i \frac{\partial}{\partial t} \psi(\mathbf{r}, t) = \underbrace{\left[-\frac{\hbar^2}{2m} \nabla^2 - \Omega L_z \right]}_{T} \psi(\mathbf{r}, t) \tag{3.28}$$

and potential parts

$$i \frac{\partial}{\partial t} \psi(\mathbf{r}, t) = \underbrace{\left[V_{ext} + g|\psi|^2 + \Phi_{dd} + g_{qf}|\psi|^3 \right]}_{V} \psi(\mathbf{r}, t) \tag{3.29}$$

that have to computed in the same time-step, dt.

Equation 3.28 can be expanded

$$i \frac{\partial}{\partial t} \psi(\mathbf{r}, t) = \left[\frac{-\hbar^2}{2m} \left(\frac{\partial^2}{\partial x^2} + \frac{\partial^2}{\partial y^2} + \frac{\partial^2}{\partial z^2} \right) + \Omega \left(y \frac{\partial}{\partial x} - x \frac{\partial}{\partial y} \right) \right] \psi(\mathbf{r}, t) \tag{3.30}$$

[1] For a time-independent potential.

and evaluated with the application of a Fourier transform[2] $\mathcal{F}$. However, a 3D $\mathcal{F}$ will not decouple $\mathcal{F}\left(y\frac{\partial}{\partial x}\psi(\mathbf{r},t)\right)$. Instead two successive 1D $\mathcal{F}$ in x,z are taken, y will be constant for $\mathcal{F}_{x,z}$ and can be removed from the Fourier transform. Similarly, for $\mathcal{F}\left(x\frac{\partial}{\partial y}\psi(\mathbf{r},t)\right)$.

Equation 3.30 is split, via the alternating direction implicit (ADI) method, into

$$i\frac{\partial}{\partial t}\psi(\mathbf{r},t) = \left(\frac{-1}{2}\frac{\partial^2}{\partial^2 x} + \frac{-1}{4}\frac{\partial^2}{\partial^2 z} - i\Omega y\frac{\partial}{\partial x}\right)\psi(\mathbf{r},t) \tag{3.31}$$

$$i\frac{\partial}{\partial t}\psi(\mathbf{r},t) = \left(\frac{-1}{2}\frac{\partial^2}{\partial^2 y} + \frac{-1}{4}\frac{\partial^2}{\partial^2 z} + i\Omega x\frac{\partial}{\partial y}\right)\psi(\mathbf{r},t) \tag{3.32}$$

that also have to be computed in the same time-step.

We evaluate $\mathcal{F}_{x,z}\psi(\mathbf{r},t)$, for a fixed y, through the decomposition

$$\psi(x,y,z,t) = \sum_s\sum_p \Psi_{ps}(y,t)e^{i\mu_p(x-a)}e^{i\gamma_p(z-e)} \tag{3.33}$$

where $\mu_p = \frac{2\pi\times p}{b-a}$, $\gamma_s = \frac{2\pi\times s}{f-e}$ are the spatial discretisation along x and z. Ψ_{ps} is the Fourier coefficient p-th mode in the x direction and s-th mode in the z direction.

Inserting into 3.31 gives a linear ordinary differential equation

$$i\frac{\partial}{\partial t}\Psi_{ps}(y,t) = \left[\frac{1}{4}\mu_p^2 + \frac{1}{8}\gamma_s^2 + \frac{1}{2}\Omega y\mu_p\right]\Psi_{ps}(y,t) \tag{3.34}$$

which can be integrated in time *exactly*

$$\Psi_{ps}(y,t) = \underbrace{e^{-i\frac{1}{8}\left[2\mu_p^2+\gamma_s^2+4\Omega y\mu_p\right]dt}}_{e^{\frac{1}{4}\cdot\frac{-i}{2\hbar}tT}}\Psi_{ps}(y,t_n) \tag{3.35}$$

where $t_n \in [t, t+dt]$.

Replacing 3.35 in the decomposition 3.33 we have the first step of Strang splitting

$$\psi^{(1)}(x_j,y_k,z_l) = \sum_p\sum_s e^{-i\frac{1}{8}\left[2\mu_p^2+\gamma_s^2+4\Omega y_k\mu_p\right]dt}(\psi_k^n)_{ps}e^{i\mu_p(x_j-a)}e^{i\gamma_p(z_l-e)} \tag{3.36}$$

j,k,l are integers that run from 0 to the max grid size for the respective dimension.

Evaluation of $\mathcal{F}_{y,z}\psi(x,t)$, for a fixed x, will lead to a similar result

$$\psi^{(2)}(x_j,y_k,z_l) = \sum_q\sum_s e^{-i\frac{1}{8}\left[2\lambda_q^2+\gamma_s^2-4\Omega x_j\lambda_q\right]dt}(\psi_j^1)_{qs}e^{i\lambda_q(y_k-c)}e^{i\gamma_p(z_l-e)} \tag{3.37}$$

[2]We can use the property $\mathcal{F}\left[\frac{d}{dx}\right]^n f(x) = (-ik_x)^n\mathcal{F}(f)$

where $\lambda_q = \frac{2\pi \times q}{d-c}$.

We have completed the application of first Strang splitting term on the initial state $\psi(x,t)$. Now, we compute the middle term of 3.27, the potential term

$$\psi^{(3)}(x_j, y_k, z_l) = e^{-idt\left[V_{ext}+g|\psi^{(2)}|^2+(V_{dd}*|\psi^{(2)}|^2)+g_{qf}|\psi^{(2)}|^3\right]}\psi^{(2)}(x_j, y_k, z_l) \tag{3.38}$$

Now, the Fourier decomposition steps outlined for 3.31 are repeated for 3.32. The final result of those operations will be the initial state $\psi(\mathbf{r},t)$ time-evolved to $\psi(\mathbf{r}, t+dt)$.

Chapter 4

Results

4.1 Verification

After implementing the rotating term, we validate the accuracy of ground states by comparing them with those obtained in Example 4.6 of [6]. The comparison involves a symmetric trap with $\omega_{trap} = 2\pi \times [100, 100, 100]$, atom number 75×10^3, final grid size of $[128, 128, 128]$, and interaction strengths $a_s = 6.3578a_0$, $a_{dd} = 0.9(a_s) = 5.7220a_0$, $a_{dd} = 0.5(a_s) = 3.1789a_0$ [1]. We specifically focus on examples with dipole orientation in the z-direction.

We were able to reproduce these results, with good agreement, by configuring the same parameters as shown in Figure 4.1.

[1] $a_0 = 5.291772x10^{-11}m$

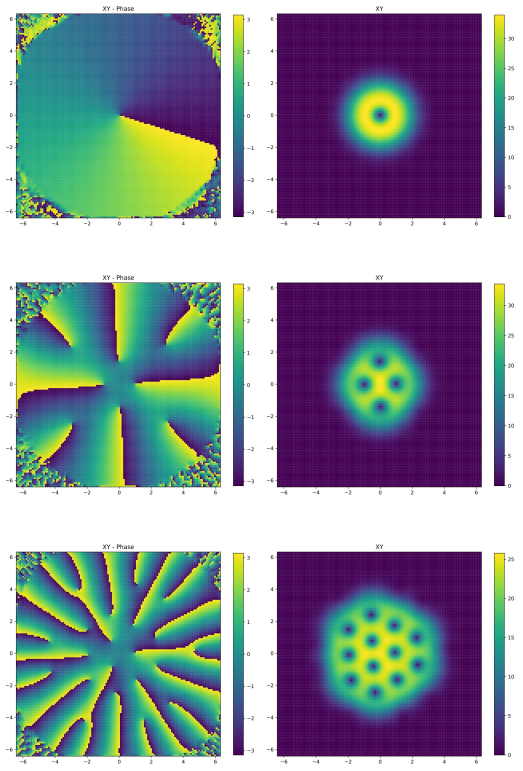

FIGURE 4.1: Phase and Density plots in the XY plane (left to right). $\Omega = 0.8\omega_{trap}$, $\Omega = 0.7\omega_{trap}$, and $\Omega = 0.9\omega_{trap}$ (top to bottom). The x-axis is in μm, and density is in $10^{21} m^{-3}$. Run times: 1538 s, 41614 s, and 41970 s respectively.

The increased convergence times compared to Example 4.6 of [6] in Figure 4.1 are attributed to using a random noise initial state and the standard conjugate gradient method, as opposed to the cascading grid method. Moreover, these vortex ground states serve as development of the cascadic multigrid method.

4.2 Cascadic Multigrid Method

A method to speed up ground state search is the implementation of the *cascadic multigrid* method (CMM) [6]. Initial guesses for ψ are generally Guassian functions, with an imposed phase. However, for fast rotating systems these produce large convergence times. The CMM process involves a series of steps to efficiently solve a problem on a grid with increasing resolution. It begins with a coarse mesh grid of size $N_p \times N_p = 2^p \times 2^p$. A ground-state search is performed on this coarse mesh grid using standard preconditions and initial data, resulting in a computed GS solution denoted as ϕ_g^p. This ground state exhibits a relatively efficient computational time expenditure. On course grids vortices are often, close to, optimally arranged and serves as a significantly better initial guess for finer grids. The mesh is then refined by doubling the grid size to $N_{p+1} \times N_{p+1}$. The solution ϕ_g^p is interpolated onto the new mesh. Applying the PCG method to solve the problem on the refined mesh produces a new computed ground state solution ϕ_g^{p+1}. These steps are repeated iteratively, incrementing p and doubling the grid size ($N_p \times N_p$) until the desired resolution $N \times N$ is achieved.

We repeatedly generate the previously identified vortex ground-states, commencing from diverse initial states outlined in Appendix C. Utilizing a starting state that encompasses a vortex significantly expedites the process. We observe that the CMM generally demonstrates accelerated convergence, and never reaches the maximum step limit of 2×10^5. For the vortex lattice case in Figure 4.4, the larger number of steps is compensated by faster convergence times.

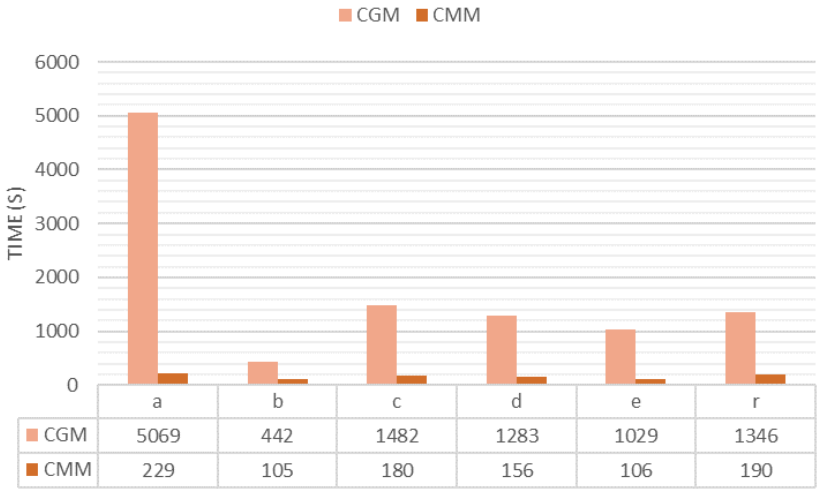

	a	b	c	d	e	r
CGM	5069	442	1482	1283	1029	1346
CMM	229	105	180	156	106	190

(A) Run Times (in s)

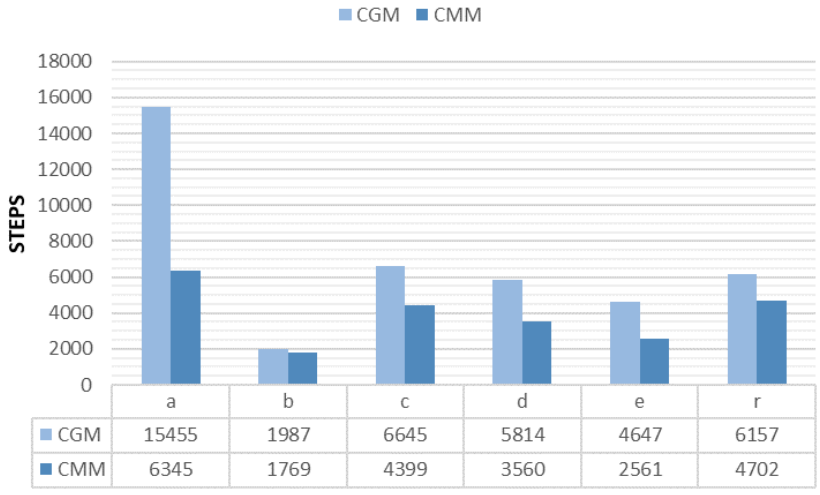

	a	b	c	d	e	r
CGM	15455	1987	6645	5814	4647	6157
CMM	6345	1769	4399	3560	2561	4702

(B) Total Steps

FIGURE 4.2: Single Vortex Ground-state. All final energies varied by less than 10^{-14}

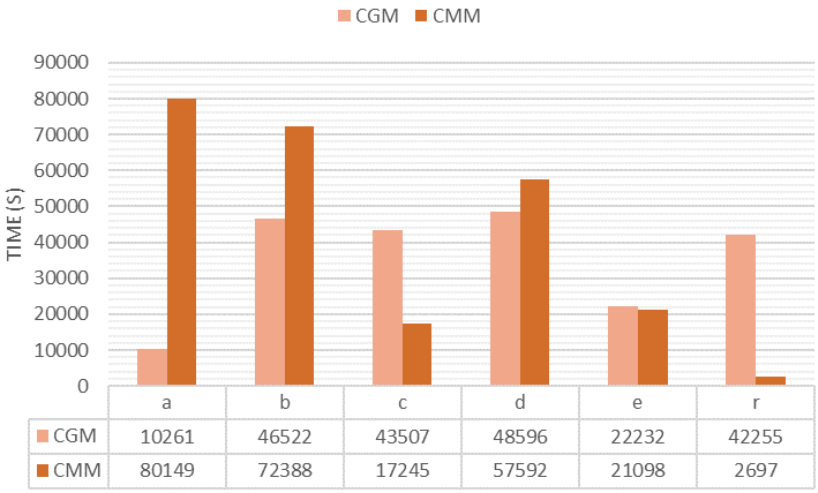

	a	b	c	d	e	r
CGM	10261	46522	43507	48596	22232	42255
CMM	80149	72388	17245	57592	21098	2697

(A) Run Times (in s)

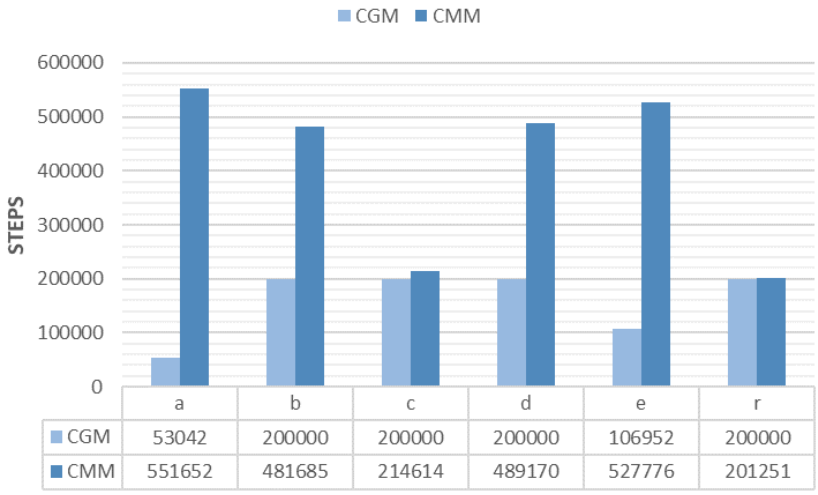

	a	b	c	d	e	r
CGM	53042	200000	200000	200000	106952	200000
CMM	551652	481685	214614	489170	527776	201251

(B) Total Steps

FIGURE 4.3: Four Vortex Ground-state. All final energies varied by less than 10^{-8}

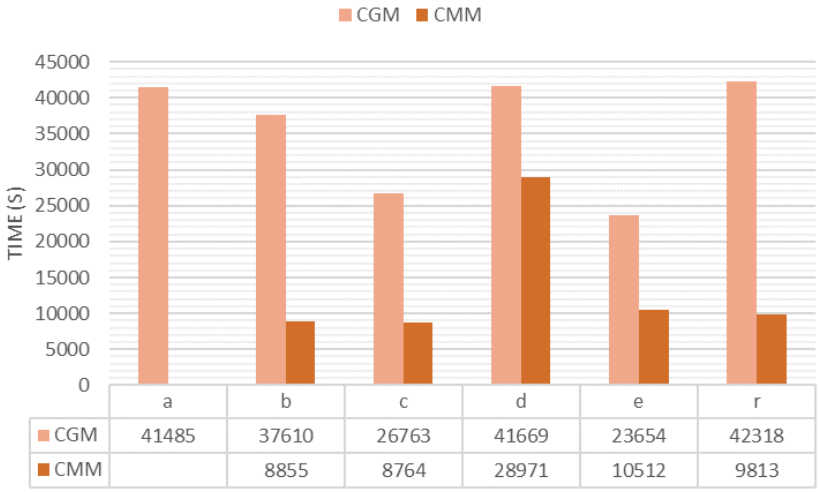

	a	b	c	d	e	r
CGM	41485	37610	26763	41669	23654	42318
CMM		8855	8764	28971	10512	9813

(A) Run Times (in s)

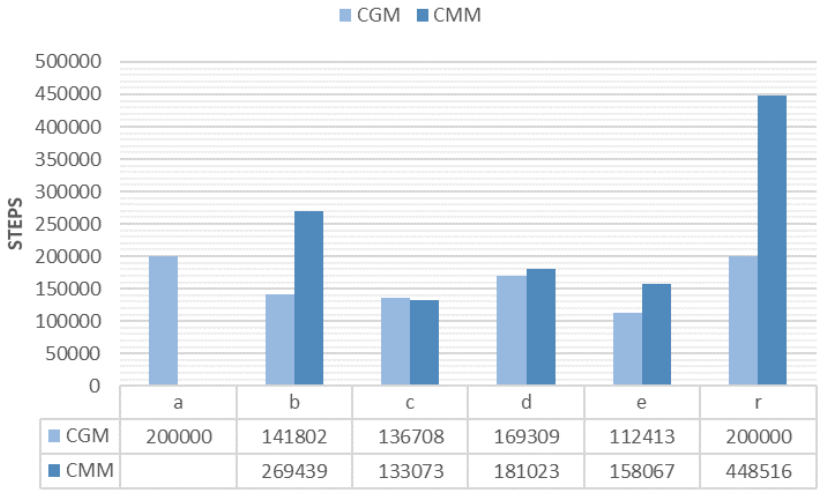

	a	b	c	d	e	r
CGM	200000	141802	136708	169309	112413	200000
CMM		269439	133073	181023	158067	448516

(B) Total Steps in the CGM

FIGURE 4.4: Vortex Lattice Ground-state. All final energies varied by less than 10^{-5}

4.3 Preconditioners

Preconditioners tested were adapted from [6, 5].

The *Kinetic Energy preconditioner*, labeled "Pki",

$$P_\Delta = \left(\alpha_\Delta - \frac{\Delta}{2}\right)^{-1} \tag{4.1}$$

α_Δ is the positive shifting constant

$$\alpha_\Delta = \tilde{\mu} = -\frac{1}{2}\langle\psi_n, \Delta\psi_n\rangle + \left\langle V_{ext}, |\psi_n|^2\right\rangle + g_s\left\langle |\psi_n|^2, |\psi_n|^2\right\rangle + \left|g_{dd}\left\langle\psi_n, |\psi_n|^2\right\rangle\right| \tag{4.2}$$

The *Potential-Interaction preconditioner*, labeled "Ppo",

$$P_V = \left(\alpha_V + V_{ext} + g_s|\psi_n|^2 + |g_{dd}|\left(1 + \text{sign}\left(\Phi_n\right)\right)\frac{\Phi_n}{2}\right)^{-1} \tag{4.3}$$

with $\alpha_V = \tilde{\mu}$.

The *Combined 1 preconditioner*, labeled "PC1" and *Combined 2 preconditioner*, labeled "PC2", as a combination of the previous preconditioners

$$P_{C_1} = P_V^{1/2} P_\Delta P_V^{1/2}; P_{C_2} = P_\Delta^{1/2} P_V P_\Delta^{1/2} \tag{4.4}$$

The *Laplace preconditioner*, labeled "Pla",

$$P_{La} = P_V P_\Delta \tag{4.5}$$

The *Ronen Kinetic preconditioner*, adapted from S. Ronen [36], labeled "PRK", where $\alpha = \max(\langle\psi_n, \psi_n\rangle, \langle\psi_n, \Delta\psi_n\rangle)$

and the identity preconditioner, "Pi", $P_I = \mathbb{1}$

Ground state searches were conducted with initial state "b", Gaussian with phase imprinting and random noise, "r".

For the single vortex case, preconditioning had a minimal effect, convergence times were 103.39s, with standard deviation 1.86, and 118.63, with standard deviation 1.55, for initial states "b" and "r" respectively. Results table in Appendix C.

Results for the four vortex case and vortex lattice case are reported in Figures 4.5, 4.6. Performance for all preconditioners in the vortex lattice state differed minimally from the identity operator. The Ronen Kinetic preconditioner showed significant improvement in the four vortex case.

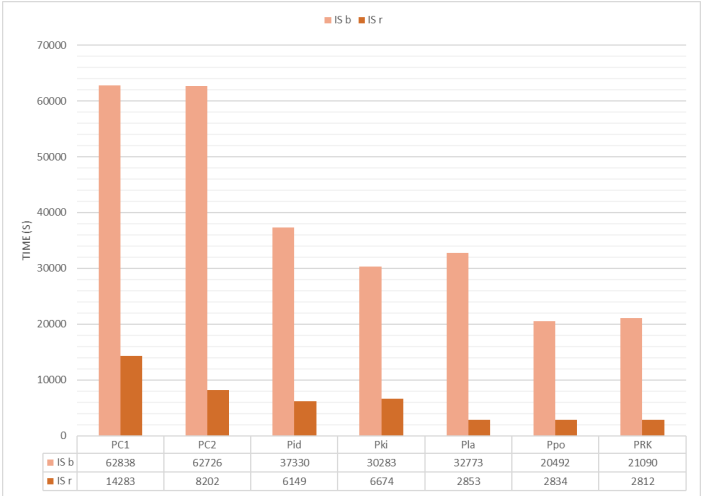

FIGURE 4.5: Run Times (in s) for Four Vortex

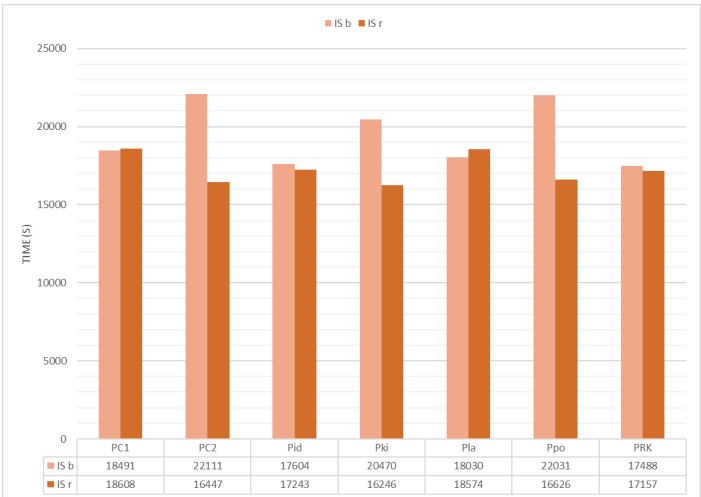

FIGURE 4.6: Run Times (in s) for Vortex Lattice

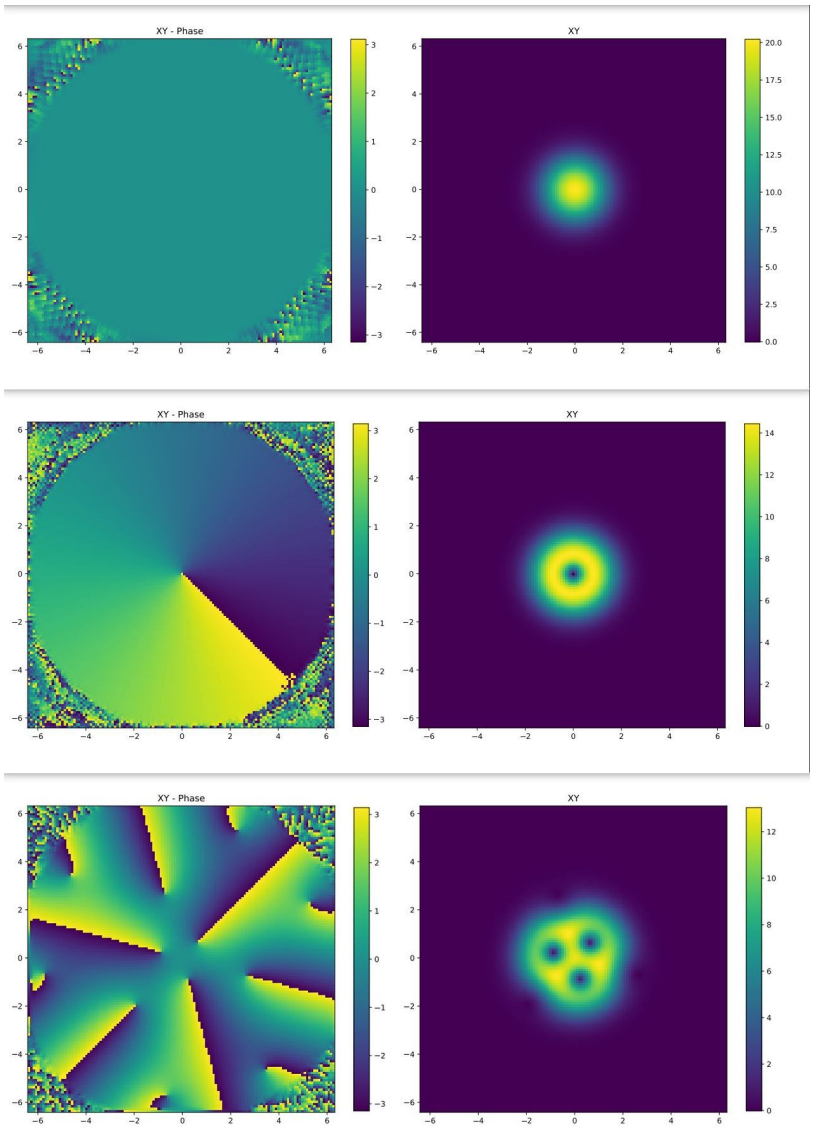

FIGURE 4.7: (Top to Bottom) No Vortex Ground-state, Single Vortex Ground State, Three Vortex Ground-state. The x-axis is in μm, and density is in $10^{21} m^{-3}$. Image from [128, 128, 128] grid.

4.4 Spatial Resolution Error

Numerical models often are tasked with conducting ground state searches across for a large range of atom numbers, scattering lengths and trap configurations to chart the boundary between phases or search for new ones. We look at the difference between $\langle E_{tot} \rangle$ for ground-states of grid sizes $[32, 32, 32]$, $[64, 64, 64]$, $[128, 128, 128]$. Three values of $\Omega = 0.75\omega_{trap}, 0.88\omega_{trap}, 0.95\omega_{trap}$ were selected, Figure 4.7. Atom number $N = 5000$, trap frequency $\omega_{trap} = 2\pi \times [100, 100, 100]$, $a_s = 6.3578 a_0$, $a_{dd} = 5.7220 a_0$.

We present $\langle E_{\text{tot}} \rangle$ values for a $[128, 128, 128]$ grid, and deviations of $\langle E_{\text{tot}} \rangle$ for grid sizes of $[32, 32, 32]$ and $[64, 64, 64]$ in Tables 4.1, 4.2, and 4.3. $\langle E_{\text{tot}} \rangle$ denotes energy per particle in units of 100 Hz. Notably, the ground state energies for $\Omega = 0.75\omega_{\text{trap}}$ and $0.88\omega_{\text{trap}}$ exhibit good agreement. However, a more pronounced error is observed for $0.95\omega_{\text{trap}}$ due to the presence of multiple vortices.

IS	$\langle E_{\mathbf{tot}} \rangle$ Deviation for G32	$\langle E_{\mathbf{tot}} \rangle$ Deviation for G64	$\langle E_{tot} \rangle$ for G128
a	-3.90E-07	2.98E-14	2.02390591702593
b	-3.90E-07	2.98E-14	2.02390591702593
c	-3.90E-07	2.00E-14	2.02390591702593
e	-3.90E-07	1.02E-14	2.02390591702592
n	-3.90E-07	2.98E-14	2.02390591702593

TABLE 4.1: Difference in $\langle E_{tot} \rangle$ between $[128, 128, 128]$ and $[32, 32, 32]$ and $[64, 64, 64]$ for the ground state of $\Omega = 0.88\omega_{trap}$. $\langle E_{\text{tot}} \rangle$ energy per particle in units of 100 Hz

IS	$\langle E_{\mathbf{tot}} \rangle$ Deviation for G32	$\langle E_{\mathbf{tot}} \rangle$ Deviation for G64	$\langle E_{tot} \rangle$ for G128
a	-1.57E-06	9.99E-15	1.99955567917781
b	-1.57E-06	0.00E+00	1.99955567917781
c	-1.57E-06	0.00E+00	1.99955567917781
e	-1.57E-06	9.99E-15	1.99955567917781
n	-1.57E-06	9.99E-15	1.99955567917782

TABLE 4.2: Difference in $\langle E_{tot} \rangle$ between $[128, 128, 128]$ and $[32, 32, 32]$ and $[64, 64, 64]$ for the ground state of $\Omega = 0.75\omega_{trap}$. $\langle E_{\text{tot}} \rangle$ energy per particle in units of 100 Hz

IS	$\langle E_{\mathbf{tot}} \rangle$ Deviation for G32	$\langle E_{\mathbf{tot}} \rangle$ Deviation for G64	$\langle E_{tot} \rangle$ for G128
a	-7.88E-07	1.91E-11	1.90454298833922
b	-6.38E-07	1.92E-11	1.90454298833924
c	-6.21E-07	1.92E-11	1.90454298833899
e	-1.32E-06	1.86E-11	1.90454298833872
n	-6.18E-07	1.92E-11	1.90454298833929

TABLE 4.3: Difference in $\langle E_{tot} \rangle$ between $[128, 128, 128]$ and $[32, 32, 32]$ and $[64, 64, 64]$ for the ground state of $\Omega = 0.95\omega_{trap}$. $\langle E_{\text{tot}} \rangle$ energy per particle in units of 100 Hz

4.5 Comparison with ITE

As a further test to confirm the correct implementation of the ground state search with rotation using CG, we implement rotation in ITE. The agreement with literature and the agreement between both methods shows that both algorithms are implemented correctly. The time evolution algorithm for the ground state search can be easily adapted for real time evolution with minor modifications.

Due to the addition of rotating term we find that the convergence times ground states via imaginary time evolution exceed $2x10^5$, even for non-vortex examples. We are able to test if the ground state convergences through the ITE by loading ground-states found via CGM as initial states in the ITE. We find that only for $dt < 10^{-6}$ the loaded state converge to a ground-state, larger values of dt result in a increase of the final ground-state energy.

	Loaded State (via CGM)	**ITE**	**Error (ITE - CGM)**
$\langle \mu \rangle$	$2.14442334913674 \times 10^{0}$	$2.14442336374844 \times 10^{0}$	$1.46116998500645 \times 10^{-8}$
$\langle E_{tot} \rangle$	$1.90454298833929 \times 10^{0}$	$1.90454298833926 \times 10^{0}$	$-2.99760216648792 \times 10^{-14}$
$\langle E_{kin} \rangle$	$1.78097986970094 \times 10^{0}$	$1.78097977132795 \times 10^{0}$	$-9.83729899761698 \times 10^{-8}$
$\langle E_{ext} \rangle$	$2.14080042894980 \times 10^{0}$	$2.14080024400850 \times 10^{0}$	$-1.84941300052088 \times 10^{-7}$
$\langle E_{con} \rangle$	$1.97816297904632 \times 10^{-1}$	$1.97816315523977 \times 10^{-1}$	$1.76193449830109 \times 10^{-8}$
$\langle E_{dip} \rangle$	$4.20640628928162 \times 10^{-2}$	$4.20640598852046 \times 10^{-2}$	$-3.00761160421104 \times 10^{-9}$
$\langle E_{rot} \rangle$	$-2.25711767110889 \times 10^{0}$	$-2.25711740240638 \times 10^{0}$	$2.68702510020091 \times 10^{-7}$

TABLE 4.4: Totals Steps taken by ITE 10^5 with $dt = 10^{-6}$. We note that the total energy value remains almost constant but values of $\langle E_{con} \rangle$ and $\langle E_{rot} \rangle$ increase proportional to the decrease of other expectation values.

Chapter 5

Conclusion and Outlook

In this thesis, we formulated numerical approaches to simulate a rotating dipolar Bose-Einstein condensate. We successfully validated our results against existing literature and also compared distinct the two ground-state search methods, demonstrating their consistent effectiveness.

Simulations in this thesis primarily focused on symmetric traps. However, exploring different trap geometries, especially those with strong confinement in the z direction, may yield intriguing results due to the quasi-2D nature of the traps.

Previous research has investigated structured forms of dipolar BECs under oblate traps [23]. Exploring the influence of rotation on these phases of matter could lead to the discovery of new ground-state arrangements and extend the general phase diagram of dipolar gases under a range of conditions.

Recent studies have delved into collective excitations described by Bogoliubov theory for ground states of self-bound droplets in a dipolar BEC [12]. Investigating the influence of rotation on these excitations is may lead to further insights about the nature of self-bound droplets.

Experiments have reported the observation of supersolidity in dipolar Bose-Einstein condensates. Although quantized vortices are challenging to observe in the supersolid phase due to low-density regions, transitioning to a purely superfluid phase allows vortex observation [37]. Simulations can be used to find suitable experimental parameters.

The effects of introducing ellipticity by breaking radial trap symmetry on vortex nucleation can be explored. Additionally, angular momentum can be induced into a dipolar system through magneto-stirring [13].

New trapping potential for BECs, like uniform box potentials [21], have been realised. Dipolar systems confined in such traps exhibit an accumulation of high density at the edges, due to their anisotropic nature [35]. Rotation under these conditions may result in unique ground-state configurations of vortices.

Further improvements to numerical methods are possible. Employing Rotating Lagrangian Coordinates to model the dynamics of a rotating BEC may be less computationally intensive [9].

Appendix A

Code Snippets

StrangSplittingKineticLz

```
function doEvolutionStep_StrangSplittingKineticLz(obj)

        KinLzX_temp = exp(0.5 * obj.gevo * ( ...
        -0.50 * (-1.0 * obj.Kx .* obj.Kx) + ...
        -0.25 * (-1.0 * obj.Kz .* obj.Kz) + ...
        -1.0i * obj.grot * obj.Ry .* (-1.0i * obj.Kx) ));



        KinLzY_temp = exp(0.5 * obj.gevo * ( ...
        -0.50 * (-1.0 * obj.Ky .* obj.Ky) + ...
        -0.25 * (-1.0 * obj.Kz .* obj.Kz) + ...
        1.0i * obj.grot * obj.Rx .* (-1.0i * obj.Ky)));



        % First Step, X
        phiKxz = fft(fft(obj.psi_time,[],3), [], 1); %z then
            x

        obj.psi_time = ifft(ifft(KinLzX_temp .* phiKxz, [],
            1),[], 3);

        % Second Step, Y
        phiKyz = fft(fft(obj.psi_time,[],3), [], 2); %z then
            y

        obj.psi_time = ifft(ifft(KinLzY_temp .* phiKyz, [],
            2),[], 3);

        % Thrid Step, Middle
        % evolution ~ |psi| (middle)
        obj.psin = abs(obj.psi_time).^2;
        obj.psid = obj.convolve(obj.psin, obj.Vdip);
        obj.psi_time = obj.psi_time .* exp( obj.gevo.*( obj.
            Vext + obj.gd*obj.psid ...
```

```
        + obj.psin.*(obj.gs + real(obj.gqf) .* sqrt(obj.psin)
            ) ));


        % Fourth Step, Y
        phiKyz = fft(fft(obj.psi_time,[],3), [], 2); %z then
            y

        obj.psi_time = ifft(ifft(KinLzY_temp .* phiKyz, [],
            2),[], 3);

        % Fifth Step, X
        phiKxz = fft(fft(obj.psi_time,[],3), [], 1); %z then
            x

        obj.psi_time = ifft(ifft(KinLzX_temp .* phiKxz, [],
            1),[], 3);


end
```

```
function doEvolutionStep_StrangSplittingKineticLz_streamlined
    (obj)

% First Step, X
phiKxz = fft(fft(obj.psi_time,[],1), [], 3); %x then z

obj.psi_time = ifft(obj.KinLzX .* phiKxz, [], 1); % keep z in
    Fspace

% Second Step, Y
phiKyz = fft(obj.psi_time,[],2); % bring y to Fspace

obj.psi_time = ifft(ifft(obj.KinLzY .* phiKyz, [], 2),[], 3);
    % y,z into Rspace

% Thrid Step, Middle
% evolution ~ |psi| (middle)
obj.psin = abs(obj.psi_time).^2;
obj.psid = obj.convolve(obj.psin, obj.Vdip);
obj.psi_time = obj.psi_time .* exp( obj.gevo.*( obj.Vext +
    obj.gd*obj.psid ...
+ obj.psin.*(obj.gs + real(obj.gqf) .* sqrt(obj.psin)) ));


% Fourth Step, Y
phiKyz = fft(fft(obj.psi_time,[],2), [], 3); %z then y

obj.psi_time = ifft(obj.KinLzY .* phiKyz, [], 2); % keep z in
    Fspace

```

```
% Fifth Step, X
phiKxz = fft(obj.psi_time,[],1); % bring z to Fspace

obj.psi_time = ifft(ifft(obj.KinLzX .* phiKxz, [], 1),[], 3);
    % x,z into Rspace

end
```

```
function LzPhi = Lz(obj, phi)
        phiK = fftn(phi);
        LzPhi = -1.0i * (obj.Rx .* ifftn( 1.0i * obj.Ky .*
           phiK ) - obj.Ry .* ifftn( 1.0i * obj.Kx .* phiK ))
           ;
end
```

Appendix B

doAys

Introduction

This document provides a detailed walkthrough of the Python code "doAys" that was developed for data analysis during this thesis. The code is organized into a class named "Analysis" and various helper functions.

The "Analysis" class takes a file path as input. The control dictionary is used to specify which parts of the analysis should be performed. If not provided, default control settings are determined based on the file name. A naming convention is followed, where ground-states found via CGM begin with 'CGM', otherwise 'fGS'.

In the constructor's initialization section, the code extracts the file name from the given path and then calls the "detMethod" method to determine the analysis method (either 'CG' or 'fGS') based on the file name prefix.

File Paths

```
1         # From the MATLAB output folder read the following
              files
2         self.file = file + "/GPEGrids3D.h5"
3         self.file_info = file + "/info.json"
4         self.file_CGM = file + "/CGmonitor.csv"
5         self.file_CGI = file + "/CGinfo.csv"
6         self.file_convcrit = file + "/statsConvcrit.csv"
```

The code constructs file paths for various data files within the provided folder. These files include simulation data in HDF5 format ('GPEGrids3D.h5'), simulation information in JSON format ('info.json'), data from the CG method in ('CGmonitor.csv') and ('CGinfo.csv'), and convergence criteria statistics ('statsConvcrit.csv'). Unless a ground-state has been loaded, only one of CGmonitor or statsConvcrit will be populated.

Control Settings

```
1         # Control is a list of bools that decides what is run
              in the _init_ func
2         # The way CGm and fGS methods store the results is
              different, and this 'control'
3         # method prevents unexpected errors.
```

```
        # The control method is set by looking at the name of
            the input file

        if control is None:
        if self.method == 'fGS':
        control_gs = {
                "h5": True,  # Needed for: plotting
                "info": True,  # Not needed but used in
                    plotting
                "CGe": False,  # Needed for: CGm energy
                "CGi": False,  # Needed for CGm energy
                "Conv": True,  # Needed for: fGS energy
        }
        control = control_gs

        if self.method == 'CG':
        control_cg = {
                "h5": True,  # Needed for: plotting
                "info": True,  # Not needed but used in
                    plotting
                "CGe": True,  # Needed for: CGm energy
                "CGi": True,  # Needed for CGm energy
                "Conv": False,  # Needed for: fGS energy
        }
        control = control_cg
```

The code defines control dictionaries based on the analysis method ('CG' or 'fGS'). These control dictionaries determine which parts of the analysis will be performed. For example, if the method is 'fGS', certain options like 'CGe' and 'CGi' are set to False because they are not needed for the 'fGS' method.

Reading HDF5 Data

```
        # Stuff extracted from h5 file
        if control['h5']:
        try:
        self.data = h5py.File(self.file, 'r')  # Gets data
        except:
        print("Error in reading h5 file.")

        try:
        self.x, self.y, self.z = self.data['xax'][0], self.
            data['yax'][0], self.data['zax'][0]  # real space
            pos
        except:
        print("Error in getting (x, y, z)")

        try:
        self.kx, self.ky, self.kz = np.array(self.data['nuxAx
            '][:, 0]), np.array(self.data['nuyAx'][:, 0]), np.
            array(
```

```
15          self.data['nuzAx'][:, 0])  # k space pos
16          except:
17          print("Error in getting (kx, ky, kz)")
18
19          try:
20          self.data_real = np.array(self.data['psiReal'])
21          self.data_imag = np.array(self.data['psiImag'])
22          except:
23          print("Error in getting real/imag part of Psi")
```

If the 'h5' option is enabled in the control dictionary, the code attempts to read data from the HDF5 file. It reads information such as the axes for real and k-space positions, as well as the real and imaginary parts of the wavefunction (psi).

Reading Simulation Information

```
1           # Stuff from json file
2           if control['info']:
3           try:
4           with open(self.file_info) as f:
5           self.info = json.load(f, object_hook=lambda d:
               SimpleNamespace(**d))
6           except:
7           print("Error in reading info.json")
```

If the 'info' option is enabled in the control dictionary, the code attempts to read simulation information from the JSON file.

If either 'CGe' or 'CGi' options are enabled in the control dictionary, the code attempts to read data from the CG monitor CSV file.

Appendix C

Numerical Results

Initial States

```
function psi = setPsi_a(obj)
% Gaussian like state
a = 1/sqrt(pi);
sigma = [5.0, 5.0, 5.0];
pos = [0.0, 0.0, 0.0];
psi = obj.setGaussian(a, sigma, pos);
obj.InitialState = 'a';
end

function psi = setPsi_b(obj)
% (x+iy) into Gaussian like state
a = 1/sqrt(pi);
sigma = [5.0, 5.0, 5.0];
pos = [0.0, 0.0, 0.0];
psi = (obj.Rx + 1i.*obj.Ry) .* obj.setGaussian(a, sigma, pos)
    ;
obj.InitialState = 'b';
end

function psi = setPsi_bconj(obj)
% (x-iy) into Gaussian like state
a = 1/sqrt(pi);
sigma = [5.0, 5.0, 5.0];
pos = [0.0, 0.0, 0.0];
psi = (obj.Rx - 1i.*obj.Ry) .* obj.setGaussian(a, sigma, pos)
    ;
obj.InitialState = 'bconj';
end

function psi = setPsi_c(obj)
% (psi_a + psi_b)/||psi_a + psi_b||
psi = ((obj.setPsi_a + obj.setPsi_b)./sqrt(obj.integrate( abs
    (obj.setPsi_a + obj.setPsi_b).^2 )));
obj.InitialState = 'c';
end

```

```
34 function psi = setPsi_cconj(obj) % confirm that cong(Psi_c)
       is same as just taking conj(Psi_b)
35 % conj((psi_a + psi_b)/||psi_a + psi_b||)
36 psi = ((obj.setPsi_a + obj.setPsi_bconj)./sqrt(obj.integrate(
       abs(obj.setPsi_a + obj.setPsi_bconj).^2 )));
37 obj.InitialState = 'cconj';
38 end
39
40 function psi = setPsi_d(obj)
41 % ((1-w)psi_a + w*psi_b)/||(1-w)psi_a + w*psi_b||
42 w_rot = obj.get_w_rot(obj.omegaRot);
43 psi = (((1-w_rot)*obj.setPsi_a + w_rot*obj.setPsi_b)./sqrt(
       obj.integrate( abs((1-w_rot)*obj.setPsi_a + w_rot*obj.
       setPsi_b).^2 )));
44 obj.InitialState = 'd';
45 end
46
47 function psi = setPsi_dconj(obj)
48 % ((1-w)psi_a + w*psi_bconj)/||(1-w)psi_a + w*psi_bconj||
49 w_rot = obj.get_w_rot(obj.omegaRot);
50 psi = (((1-w_rot)*obj.setPsi_a + w_rot*obj.setPsi_bconj)./
       sqrt(obj.integrate( abs((1-w_rot)*obj.setPsi_a + w_rot*obj
       .setPsi_bconj).^2 )));
51 obj.InitialState = 'dconj';
52 end
53
54 function psi = setPsi_e(obj)
55 % ((1-w)psi_a + w*psi_b)/||(1-w)psi_a + w*psi_b||
56 w_rot = obj.get_w_rot(obj.omegaRot);
57 psi = ((w_rot*obj.setPsi_a + (1-w_rot)*obj.setPsi_b)./sqrt(
       obj.integrate( abs(w_rot*obj.setPsi_a + (1-w_rot)*obj.
       setPsi_b).^2 )));
58 obj.InitialState = 'e';
59 end
60
61 function psi = setPsi_econj(obj)
62 % ((1-w)psi_a + w*psi_bconj)/||(1-w)psi_a + w*psi_bconj||
63 w_rot = obj.get_w_rot(obj.omegaRot);
64 psi = ((w_rot*obj.setPsi_a + (1-w_rot)*obj.setPsi_bconj)./
       sqrt(obj.integrate( abs(w_rot*obj.setPsi_a + (1-w_rot)*obj
       .setPsi_bconj).^2 )));
65 obj.InitialState = 'econj';
66 end
```

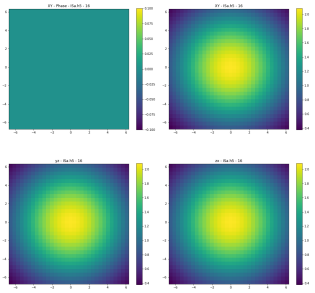

FIGURE C.1: Initial State a

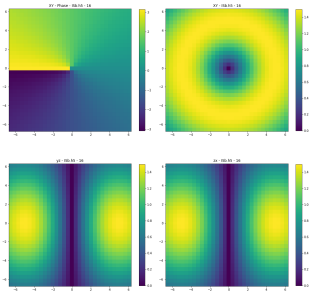

FIGURE C.2: Initial State b

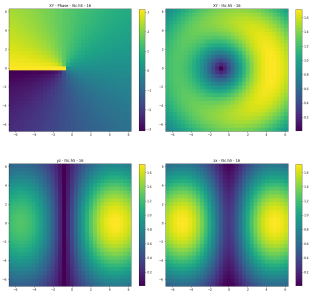

FIGURE C.3: Initial State c

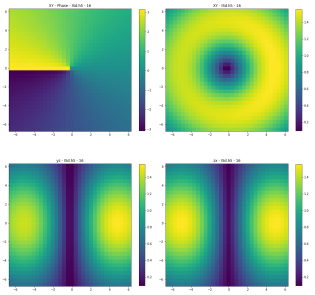

FIGURE C.4: Initial State d

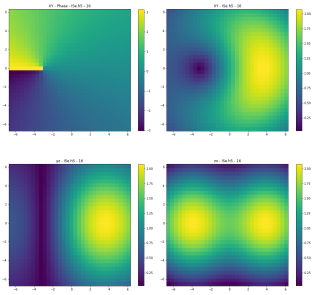

FIGURE C.5: Initial State e

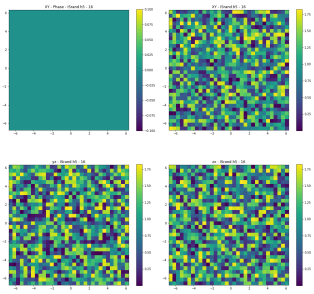

FIGURE C.6: Initial State r

Preconditioner	**Run Time (s)**
PC1	107.515928
PC2	103.736981
Pid	101.317611
Pki	103.326758
Pla	102.089074
Ppo	103.308813
PRK	103.433049

TABLE C.1: Convergence times for Single vortex ground-state, with initial state "b", with various preconditioners

Preconditioner	**Run Time (s)**
PC1	116.906329
PC2	119.640565
Pid	117.631551
Pki	118.185651
Pla	120.674358
Ppo	116.703419
PRK	118.708186

TABLE C.2: Convergence times for Single vortex ground-state, with initial state "r", with various preconditioners

References

[1] J. R. Abo-Shaeer et al. “Observation of Vortex Lattices in Bose-Einstein Condensates”. In: *Science* 292.5516 (Apr. 20, 2001), pp. 476–479. ISSN: 0036-8075, 1095-9203. DOI: 10.1126/science.1060182. URL: https://www.science.org/doi/10.1126/science.1060182 (visited on 09/28/2023).

[2] A A Abrikosov. “Magnetic properties of superconductors of the second group”. In: *Sov. Phys. - JETP (Engl. Transl.); (United States)* 5:6 (Jan. 1957). URL: https://www.osti.gov/biblio/7155233.

[3] Xavier Antoine and Romain Duboscq. “GPELab, a Matlab toolbox to solve Gross–Pitaevskii equations II: Dynamics and stochastic simulations”. In: *Computer Physics Communications* 193 (Aug. 2015), pp. 95–117. ISSN: 00104655. DOI: 10.1016/j.cpc.2015.03.012. URL: https://linkinghub.elsevier.com/retrieve/pii/S0010465515001113 (visited on 05/04/2022).

[4] Xavier Antoine and Romain Duboscq. “Modeling and computation of Bose-Einstein condensates: Stationary states, nucleation, dynamics, stochasticity”. In: *Nonlinear Optical and Atomic Systems: At the Interface of Physics and Mathematics* (2015). ISBN: 9783319190150, pp. 49–145. ISSN: 00758434. DOI: 10.1007/978-3-319-19015-0_2.

[5] Xavier Antoine, Antoine Levitt, and Qinglin Tang. “Efficient spectral computation of the stationary states of rotating Bose–Einstein condensates by preconditioned nonlinear conjugate gradient methods”. In: *Journal of Computational Physics* 343 (2017). Publisher: Elsevier Inc., pp. 92–109. ISSN: 10902716. DOI: 10.1016/j.jcp.2017.04.040. URL: http://dx.doi.org/10.1016/j.jcp.2017.04.040.

[6] Xavier Antoine, Qinglin Tang, and Yong Zhang. “A preconditioned conjugated gradient method for computing ground states of rotating dipolar bose-Einstein condensates via kernel truncation method for dipole-dipole interaction evaluation”. In: 24.4 (2018), pp. 966–988. ISSN: 19917120. DOI: 10.4208/CICP.2018.HH80.11.

[7] Xavier Antoine et al. “Acceleration of the imaginary time method for spectrally computing the stationary states of Gross–Pitaevskii equations”. In: *Computer Physics Communications* 219 (Oct. 2017), pp. 70–78. ISSN: 00104655. DOI: 10.1016/j.cpc.2017.05.008. URL: https://linkinghub.elsevier.com/retrieve/pii/S0010465517301388 (visited on 05/04/2022).

[8] Weizhu Bao, Qiang Du, and Yanzhi Zhang. “Dynamics of Rotating Bose–Einstein Condensates and its Efficient and Accurate Numerical Computation”. In: *SIAM Journal on Applied Mathematics* 66.3 (Jan. 2006), pp. 758–786. ISSN: 0036-1399, 1095-712X. DOI: 10.1137/050629392. URL: http://epubs.siam.org/doi/10.1137/050629392 (visited on 04/11/2022).

[9] Weizhu Bao et al. “A Simple and Efficient Numerical Method for Computing the Dynamics of Rotating Bose–Einstein Condensates via Rotating Lagrangian Coordinates”. In: *SIAM Journal on Scientific Computing* 35.6 (Jan. 2013), A2671–

A2695. ISSN: 1064-8275, 1095-7197. DOI: 10.1137/130911111. URL: http://epubs.siam.org/doi/10.1137/130911111 (visited on 08/12/2022).

[10] Carlo F. Barenghi and Nick G. Parker. "A primer on quantum fluids: Simulating the 1D GPE". In: 223.2004 (2016). ISBN: 9783319424767. DOI: 10.1007/978-3-319-42476-7. arXiv: 1605.09580. URL: http://arxiv.org/abs/1605.09580%0Ahttp://dx.doi.org/10.1007/978-3-319-42476-7.

[11] R. A. Battye and S. J. Cotterill. "Stable Cosmic Vortons in Bosonic Field Theory". In: *Physical Review Letters* 127.24 (2021). Publisher: American Physical Society, p. 241601. ISSN: 10797114. DOI: 10.1103/PhysRevLett.127.241601. URL: https://doi.org/10.1103/PhysRevLett.127.241601.

[12] P. Blair Blakie. *Axial collective mode of a dipolar quantum droplet*. Mar. 13, 2023. arXiv: 2303.06894[cond-mat]. URL: http://arxiv.org/abs/2303.06894 (visited on 03/16/2023).

[13] Thomas Bland et al. *Vortices in dipolar Bose-Einstein condensates*. Mar. 23, 2023. arXiv: 2303.13263[cond-mat,physics:quant-ph]. URL: http://arxiv.org/abs/2303.13263 (visited on 03/27/2023).

[14] N. Bogolubov. "ON THE THEORY OF SUPERFLUIDITY". In: *Helium 4*. Elsevier, 1971, pp. 247–267. ISBN: 978-0-08-015816-7. DOI: 10.1016/B978-0-08-015816-7.50020-1. URL: https://linkinghub.elsevier.com/retrieve/pii/B9780080158167500201 (visited on 09/29/2023).

[15] J. L. Bohn, R. M. Wilson, and S. Ronen. "How does a dipolar Bose-Einstein condensate collapse?" In: *Laser Physics* 19.4 (Apr. 2009), pp. 547–549. ISSN: 1054-660X, 1555-6611. DOI: 10.1134/S1054660X09040021. URL: http://link.springer.com/10.1134/S1054660X09040021 (visited on 03/23/2022).

[16] Fabian Böttcher et al. "Dilute dipolar quantum droplets beyond the extended Gross-Pitaevskii equation". In: *Physical Review Research* 1.3 (Nov. 8, 2019), p. 033088. ISSN: 2643-1564. DOI: 10.1103/PhysRevResearch.1.033088. URL: https://link.aps.org/doi/10.1103/PhysRevResearch.1.033088 (visited on 07/25/2022).

[17] Lauriane Chomaz et al. "Dipolar physics: A review of experiments with magnetic quantum gases". In: *arXiv:2201.02672 [cond-mat, physics:physics, physics:quant-ph]* (Jan. 7, 2022). arXiv: 2201.02672. URL: http://arxiv.org/abs/2201.02672 (visited on 03/26/2022).

[18] André Cidrim et al. "Vortices in self-bound dipolar droplets". In: *Physical Review A* 98.2 (2018), pp. 1–6. ISSN: 24699934. DOI: 10.1103/PhysRevA.98.023618. arXiv: 1710.08725.

[19] Von Der Fakult and Matthias Wenzel. "Macroscopic States of Dipolar Quantum Gases". PhD thesis. Universit¨at Stuttgart, 2018.

[20] R.P. Feynman. "Chapter II Application of Quantum Mechanics to Liquid Helium". In: *Progress in Low Temperature Physics*. Vol. 1. Elsevier, 1955, pp. 17–53. ISBN: 978-0-444-53307-4. DOI: 10.1016/S0079-6417(08)60077-3. URL: https://linkinghub.elsevier.com/retrieve/pii/S0079641708600773 (visited on 09/21/2023).

[21] Alexander L. Gaunt et al. "Bose-Einstein condensation of atoms in a uniform potential". In: *Physical Review Letters* 110.20 (May 16, 2013), p. 200406. ISSN: 0031-9007, 1079-7114. DOI: 10.1103/PhysRevLett.110.200406. arXiv: 1212.4453[cond-mat,physics:physics,physics:quant-ph]. URL: http://arxiv.org/abs/1212.4453 (visited on 09/30/2023).

[22] S. Halder et al. *Phase diagram and dynamics of ^{164}Dy dipolar Bose-Einstein condensate in the presence of a rotating anisotropic magnetic field*. Number: arXiv:2205.05193. May 10, 2022. arXiv: 2205.05193[cond-mat,physics:nlin,physics:physics,

physics:quant-ph]. URL: http://arxiv.org/abs/2205.05193 (visited on 05/14/2022).

[23] J. Hertkorn et al. "Pattern formation in quantum ferrofluids: From supersolids to superglasses". In: *Physical Review Research* 3.3 (2021), pp. 1–14. ISSN: 26431564. DOI: 10.1103/physrevresearch.3.033125. arXiv: 2103.13930.

[24] Jingjing Jin, Wei Han, and Suying Zhang. "Gauge-potential-induced rotation of spin-orbit-coupled Bose-Einstein condensates". In: (), pp. 1–7. arXiv: 1804.05700v3.

[25] Lauritz Klaus et al. *Observation of vortices and vortex stripes in a dipolar Bose-Einstein condensate*. June 24, 2022. arXiv: 2206.12265[cond-mat]. URL: http://arxiv.org/abs/2206.12265 (visited on 09/26/2022).

[26] Sebastian Kling. "Rotating Bose-Einstein Condensates Diploma Thesis of". Issue: September. PhD thesis. 2005.

[27] T. D. Lee, Kerson Huang, and C. N. Yang. "Eigenvalues and Eigenfunctions of a Bose System of Hard Spheres and Its Low-Temperature Properties". In: *Physical Review* 106.6 (June 15, 1957). Publisher: American Physical Society, pp. 1135–1145. DOI: 10.1103/PhysRev.106.1135. URL: https://link.aps.org/doi/10.1103/PhysRev.106.1135 (visited on 09/25/2023).

[28] K. W. Madison et al. "Vortex formation in a stirred bose-einstein condensate". In: *Physical Review Letters* 84.5 (2000), pp. 806–809. ISSN: 10797114. DOI: 10.1103/PhysRevLett.84.806. arXiv: cond-mat/9912015.

[29] Jan-Frederik Mennemann et al. *Optimal control of the self-bound dipolar droplet formation process*. May 29, 2019. DOI: 10.1016/j.cpc.2019.06.002. arXiv: 1905.12546[physics, physics:quant-ph]. URL: http://arxiv.org/abs/1905.12546 (visited on 08/11/2022).

[30] Koushik Mukherjee et al. "Dynamics of the Creation of a Rotating Bose–Einstein Condensation by Two Photon Raman Transition Using a Laguerre–Gaussian Laser Pulse". In: *Atoms* 9.1 (Feb. 8, 2021), p. 14. ISSN: 2218-2004. DOI: 10.3390/atoms9010014. URL: https://www.mdpi.com/2218-2004/9/1/14.

[31] L. Onsager. "Statistical hydrodynamics". In: *Il Nuovo Cimento* 6 (S2 Mar. 1949), pp. 279–287. ISSN: 0029-6341, 1827-6121. DOI: 10.1007/BF02780991. URL: http://link.springer.com/10.1007/BF02780991 (visited on 09/21/2023).

[32] Sherzod R. Otajonov. "Quantum droplets in three-dimensional Bose-Einstein condensates". In: *Journal of Physics B: Atomic, Molecular and Optical Physics* 55.8 (Apr. 20, 2022), p. 085001. ISSN: 0953-4075, 1361-6455. DOI: 10.1088/1361-6455/ac6365. arXiv: 2207.00513[cond-mat, physics:nlin]. URL: http://arxiv.org/abs/2207.00513 (visited on 08/12/2022).

[33] C. J. Pethick and H. Smith. *Bose–Einstein Condensation in Dilute Gases*. 2nd ed. Cambridge University Press, Sept. 11, 2008. ISBN: 978-0-521-84651-6 978-0-511-80285-0. DOI: 10.1017/CBO9780511802850. URL: https://www.cambridge.org/core/product/identifier/9780511802850/type/book (visited on 09/21/2023).

[34] Lev Pitaevskii and Sandro Stringari. *Bose-Einstein Condensation*. ISBN: 978-0-19-850719-2.

[35] Santo Maria Roccuzzo. "Supersolidity in a Dipolar Bose Gas". Issue: November. PhD thesis. 2021.

[36] Shai Ronen, Daniele C. E. Bortolotti, and John L. Bohn. "Bogoliubov modes of a dipolar condensate in a cylindrical trap". In: *Physical Review A* 74.1 (July 31, 2006), p. 013623. ISSN: 1050-2947, 1094-1622. DOI: 10.1103/PhysRevA.74.013623. URL: https://link.aps.org/doi/10.1103/PhysRevA.74.013623 (visited on 03/27/2022).

[37] Marija Šindik et al. *Creation and robustness of quantized vortices in a dipolar supersolid when crossing the superfluid-to-supersolid transition*. June 28, 2022. arXiv: 2206.14100[cond-mat]. URL: http://arxiv.org/abs/2206.14100 (visited on 08/09/2022).